

## Supporting Information

### **Medium-entropy ceramic aerogels for robust thermal sealing**

Shubin Fu, Dizhou Liu, Yuanpeng Deng, Menglin Li, Han Zhao, Jingran Guo, Jian Zhou,  
Pengyu Zhang, Chong Wang, Hongxuan Yu, Shixuan Dang, Jianing Zhang, Menglong Hao,  
Hui Li & Xiang Xu.

\*Corresponding author: Xiang Xu, [xuxiang@hit.edu.cn](mailto:xuxiang@hit.edu.cn); Hui Li, [lihui@hit.edu.cn](mailto:lihui@hit.edu.cn)

## Supplementary Text

### Medium-entropy ceramic design

Enhanced sampling method for phase transition simulations: Due to the high energy barrier between relevant material phases, it remains challenging to accurately reveal crystallization process with classical MD simulations on practical time scales<sup>1</sup>. To this challenge, a number of enhanced sampling methods have been developed to efficiently accelerate crystallization process in MD simulations<sup>2-4</sup>. As one of the representative enhanced sampling methods, metadynamics method generate a bias potential as function of CVs on the fly and help simulated system overcome energy barriers. To perform phase transition simulations for the medium-entropy ceramics and three kinds of traditional low-entropy ceramics, we took use of well-tempered metadynamics (WTMetaD)<sup>5</sup> enhanced sampling method with molecular dynamics (MD) simulations. WTMetaD could help the system overcome energy barriers by introducing a history dependent bias potential  $V(s,t)$ ,

$$V(s,t) = \Delta T \ln \left( 1 + \frac{\omega N(s,t)}{\Delta T} \right) \quad (\text{S1})$$

where  $\Delta T$  is a temperature which is calculated from a preselected bias factor  $\gamma = (T + \Delta T)/T$ ,  $\omega$  is the height of bias potential,  $t$  is the simulation time,  $s$  is a set of collective variables (CVs), and  $N(s,t)$  is the histogram of CVs. The bias factor  $\gamma$  was introduced to prevent the system falling into regions with much higher free energy which were not physically relevant. With WTMetaD simulation, free energy surface of four ceramic systems was estimated with histogram of CVs as follows,

$$F(s,t) = - (T + \Delta T) \ln \left( 1 + \frac{\omega N(s,t)}{\Delta T} \right) \quad (\text{S2})$$

for the study in current work, we simplified the issue by ignoring the crystallization of pure  $\text{TiO}_2$  while focus on the phase transition of  $\text{ZrO}_2$ , which showed to be the main constituent of crystalline part in the medium-entropy ceramics. To address the performance of medium-entropy ceramics, we conducted crystallization simulation for three kinds of traditional low-entropy ceramics as contrast. Specifically, we conducted phase transition simulations of  $\text{ZrO}_2$  and yttrium stabilized  $\text{ZrO}_2$  ( $(\text{Zr}_{0.83}\text{Y}_{0.17})\text{O}_{2.17}$ ) by choosing the average cubic harmonic order parameter<sup>6,7</sup> of zirconium ions as CV, which can characterize well crystallinity of monocrystalline  $\text{ZrO}_2$ . For the system with silicon and titanium, the titanium (silicon) ions may form amorphous titanium oxide (silica) outside crystalline zirconia, or rather crystallize together with zirconium ions and resulting in crystalline zirconia with lattice distortion. In order to distinguish crystalline and amorphous structures, and further separate pure crystalline

zirconia and titanium doping crystalline zirconia with lattice distortion, for the phase transition simulation of  $(\text{Zr}_{0.77}\text{Y}_{0.15}\text{Si}_{0.08})\text{O}_{2.24}$  and  $(\text{Ti}_{0.42}\text{Zr}_{0.42}\text{Y}_{0.08}\text{Si}_{0.08})\text{O}_{2.08}$ , we chose two different CVs, the number of bridging oxygen (BO) as  $S_1$ , and the dot product of local Steinhardt's order parameter<sup>8-10</sup>  $q_4^{dot}$  of zirconium as  $S_2$ . The number of BO can characterize the enrichment degree of titanium (silicon) ions. For the system with silicon and titanium, the more BO indicated that there are more titanium-silicon-rich regions, while the lower BO indicated the zirconium and titanium (silicon) ions were mixed more uniformly. As reported in previous study, the parameter  $q_l^{dot}$  can tell whether the ordered zirconium atoms were clustered together or not. By using these two CVs together, the three states that we concerned, namely, pure crystalline zirconia, titanium doping crystalline zirconia with lattice distortion, and amorphous state can be separated well with each other.

Training of machine learning potential: For multicomponent oxide ceramics, the lack of efficient and accurate classical interatomic potentials blocks MD study for inherent mechanism of crystallization and precise estimation of thermodynamics and mechanical properties. The advances in machine learning (ML) and artificial intelligence provide a new paradigm in MD simulations with ab initio accuracy<sup>11</sup>. The ML models are optimized to fit interatomic potentials from accurate data sets obtained by density functional theory (DFT) calculations. The well-trained ML potential can characterize well atomic interactions and result in precise representation of the potential energies and forces at a much lower cost compared to DFT calculations. To train efficient ML potential with ab initio accuracy representation of atomic interactions for the whole phase transition process, it is crucial to obtain all the characteristic configurations, namely crystalline structures, amorphous structures, and the structures with two phases coexist. Active learning procedure has been successively applied to the configuration collection and construction of ML potential for monoatomic systems<sup>12,13</sup>. The active learning training procedure consists of four parts, i.e. the enhanced sampling simulation, selection of candidate configurations, samples labeling, and ML potential training. However, we found that the original active learning procedure is not adaptive with multicomponent medium entropy ceramics system. To reduce the computational cost for sample labeling with DFT calculations, the atom number used in DFT calculations was limited to  $\sim 100$ . Apparently, for medium-entropy ceramic system, a candidate configuration of  $\sim 100$  atoms with equal proportion of cations contains only  $\sim 10$  atoms of each cation, which was not efficient for configurations collection of various atomic arrangement for each element. This would significantly increase the amount of data to

completely cover all the characteristic configurations and lead to too much computational cost with DFT calculations.

To better adjust multicomponent oxide ceramics and train an accurate ML potential more efficiently, we modified the procedure of active learning for ML potential training, which we would refer to as stepwise training. The work flow for the stepwise training procedure for medium-entropy ceramic system was shown in Figure S1. First, an initial ML potential was trained with configurations obtained from enhanced sampling simulation with medium-entropy ceramic system of  $(\text{Ti}_{0.42}\text{Zr}_{0.42}\text{Y}_{0.08}\text{Si}_{0.08})\text{O}_{2.08}$  by using an inaccurate classical potential. The parameters of classical BKS potential in this step were combined by the parameters for  $\text{Ti}/\text{O}^{14}$ ,  $\text{Y}/\text{O}^{15}$ , and  $\text{Zr}/\text{Si}/\text{O}^{16}$ , which was not compatible with each other. It should be mentioned that the empirical potential used for the generation of initial ML potential does not need to be particularly accurate, since all the required energy and forces of the training sets is then estimated with DFT calculations. Second, to characterize short-range interactions of each cation with oxygen atoms, we took use of the initial ML potential trained in iteration 0 and performed enhanced sampling of  $\text{ZrO}_2$ ,  $\text{SiO}_2$ ,  $\text{TiO}_2$ ,  $\text{Y}_2\text{O}_3$ , and medium-entropy ceramic system, respectively, to collect relevant configurations for the training of ML potential in iteration 1. To stepwise enlarge the training set and extend applicability of ML potential for longer range interactions, for iteration 2 and 3, we additionally performed enhanced sampling for ceramics with two types of cations (i.e.,  $\text{ZrTiO}_4$ ,  $\text{Zr}_2\text{Y}_2\text{O}_7$ , and  $\text{ZrSiO}_4$ ) and three types of cations (i.e.,  $\text{ZrTiSiO}_6$  and  $\text{Zr}_2\text{Y}_2\text{Ti}_2\text{O}_{11}$ ). For all the supplemental training set used here, the proportion of each cation are set to equal. From the fourth iterations, we only performed enhanced sampling simulations for the three traditional low-entropy ceramic systems (i.e.,  $\text{ZrO}_2$ ,  $(\text{Zr}_{0.83}\text{Y}_{0.17})\text{O}_{2.17}$ , and  $(\text{Zr}_{0.77}\text{Y}_{0.15}\text{Si}_{0.08})\text{O}_{2.24}$ ) and the medium-entropy ceramic system  $(\text{Ti}_{0.42}\text{Zr}_{0.42}\text{Y}_{0.08}\text{Si}_{0.08})\text{O}_{2.08}$ . By taking the stepwise active learning strategy, the effectiveness of ML potential increased and can characterize well atomic interactions from short to longer range. Details of the number of atoms in each configuration, and number of configurations of each system from iteration 0 to 5 was listed in Supplementary Table S1. Further, we verified the performance of final ML potential on 9 supplemental systems with equal proportion of cations as well as four final systems. The true values of atomic energy and forces obtained with DFT calculations as functions of predicted values by ML potential were demonstrated in Figure S2 and S3, while the root mean square error (RMSE) in atomic energy and forces of ML potentials were given in each plot. The

final ML potential model at final iteration show good performance on predicting atomic energy and forces for each ceramic system.

#### Fabrication details of MECA

Fabrication of PAZ: Firstly, 0.2mol (64.45g) of zirconia chloride was dissolved in 300ml of methanol to form transparent solution, and 0.2mol (20.024g) of acetylacetone and 0.4mol (40.476g) of triethylamine were dissolved in another 300ml of methanol to obtain pale yellow transparent solution. Then, the methanol solution of acetylacetone and triethylamine was atomized into zirconia chloride methanol solution under the conditions of 4-20 °C (ice bath can be used) and stirring with white smoke. After that, the mixture was continue stirred for 24h to obtain a golden yellow transparent solution containing zirconium organic polymer. Afterwards, methanol was evaporated by reduced pressure distillation under 60 °C. The PAZ was dissolved by 200mol of acetone and triethylamine hydrochloride was filtered out, and acetone was removed by reduced pressure distillation at 70 °C to obtain the yellow powder, PAZ.

Preparation of electrospinning precursor: 0.3 mol (8 g) of PAZ and 0.06 mol (2.549 g) of yttrium (III) nitrate hexahydrate were dissolved in 7 g methanol with stirring at 60 °C to obtain golden transparent solution A. 0.06 mol (1.3257 g) of (3-Aminopropyl) triethoxysilane was dissolved in another 4g methanol with stirring at 60 °C to obtain transparent solution B. 0.3mol (10.19g) of tetrabutyl titanate was dissolved in another 6g methanol with stirring at 60 °C to obtain transparent solution C. And 50 mg PEO was dissolved in 5g methanol with stirring at 60 °C for 30min to obtain transparent solution D. Then, solution B was added into A with stirring to obtain solution E. After that, solution C was added into E to obtain solution F. In the end, solution D was added into F with further stirring to form the homogeneous precursor solution.

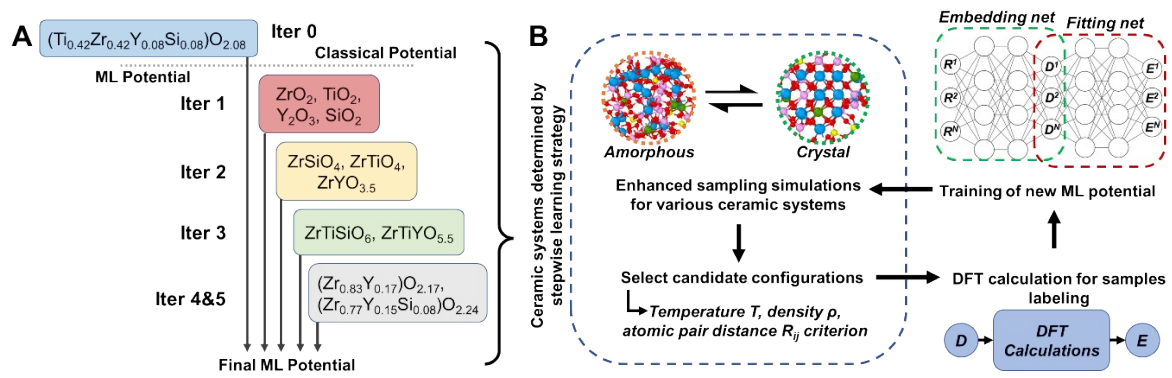


**Figure S1.**

**Work flow for the training of ML potential for medium-entropy ceramic system.** (A) A stepwise training strategy was taken to ensure the compatibility of final ML potential with each kind of atomic arrangement. The ML potential at iter 0 is trained with configurations obtained with a classical potential, while the other configurations collected in iter 1-5 were obtained with ML potential trained in previous iteration. (B) Active learning procedure for training of ML potential for medium-entropy ceramic system.

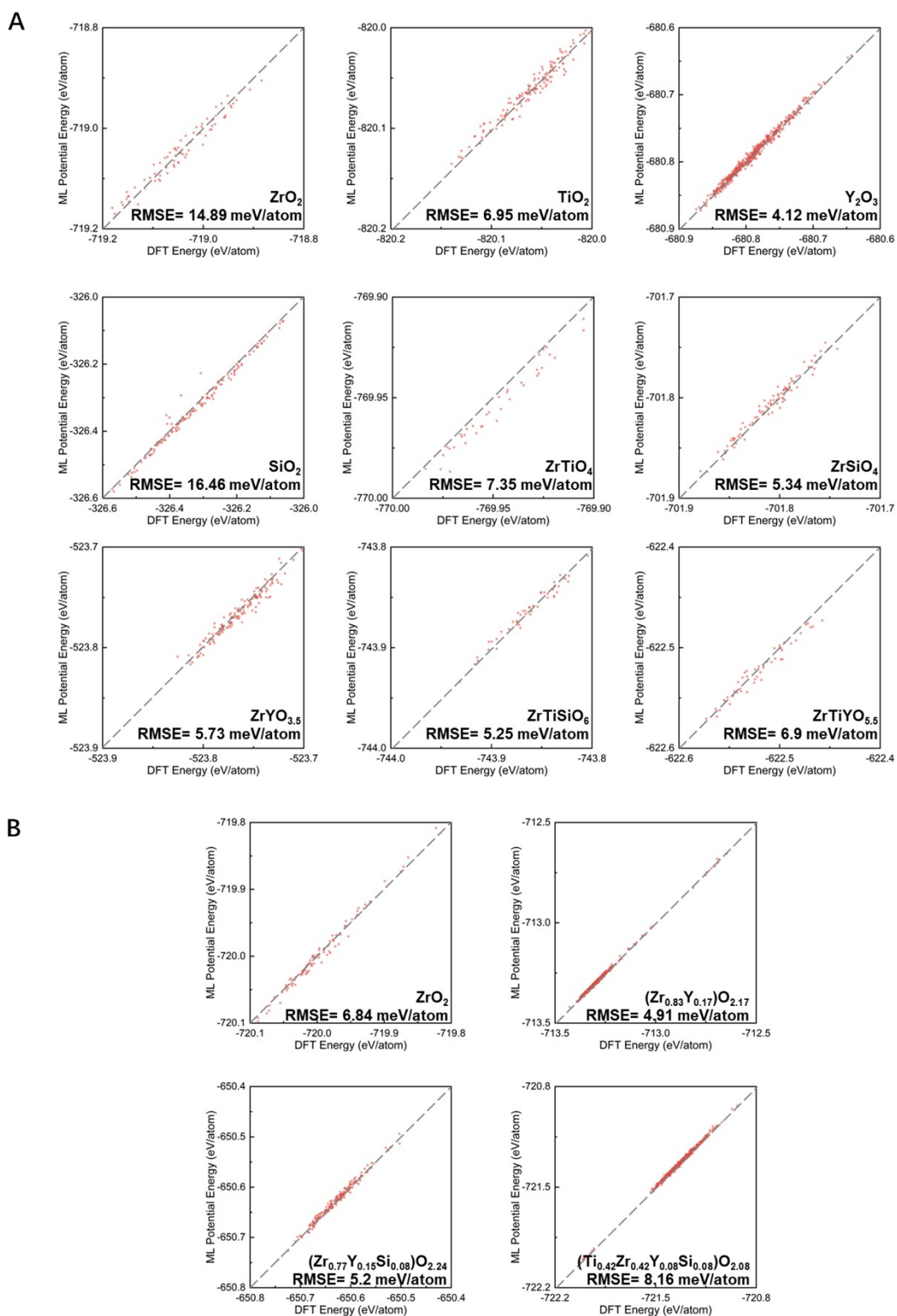


**Figure S2.**

True values of atomic energy as functions of predicted values produced by final ML potential for (A) 9 set of supplemental training sets with equal proportion of cations and (B) 4 set of systems with unequal proportion of cations.

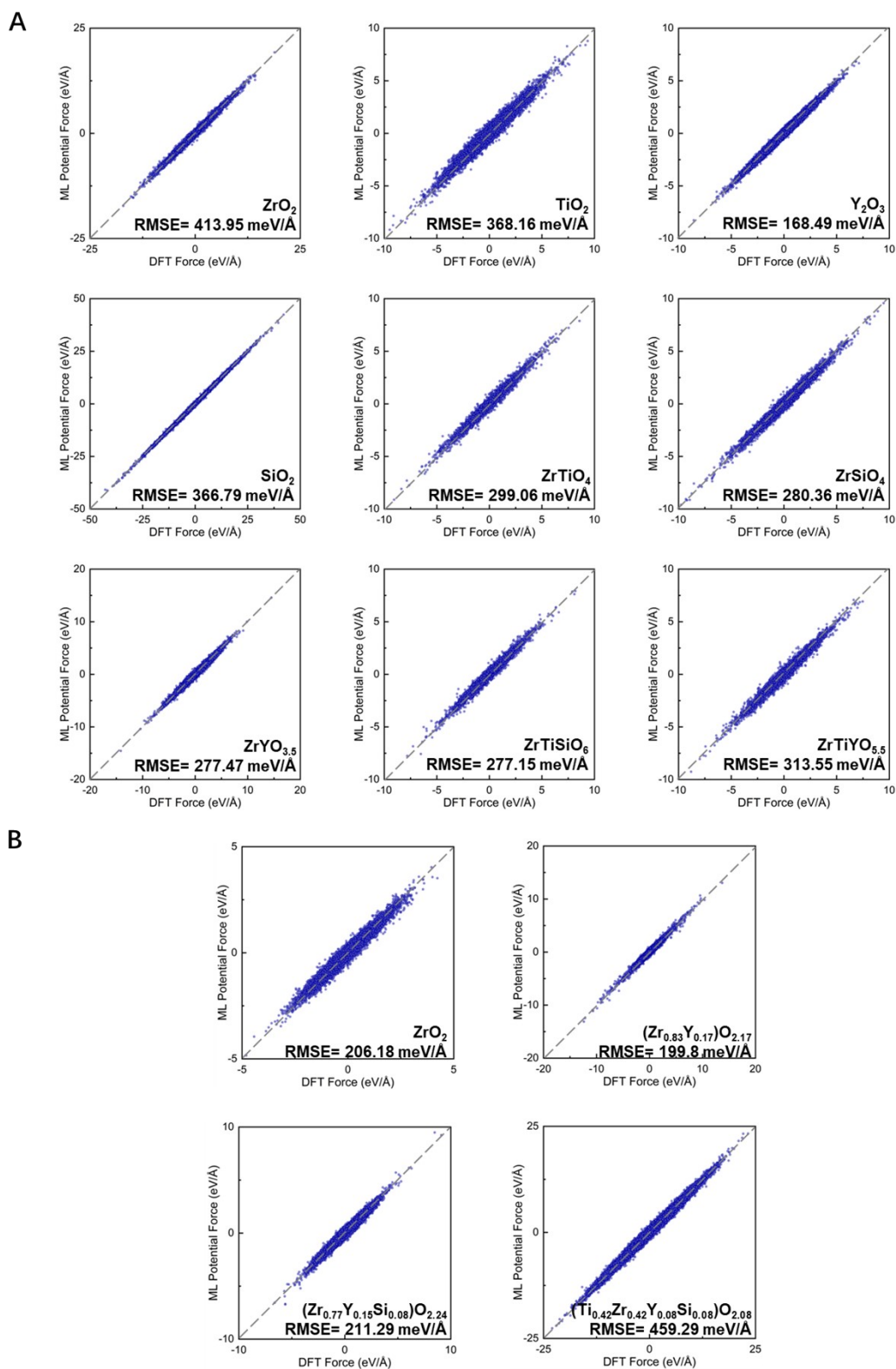


**Figure S3.**

**True values of atomic forces as functions of predicted values produced by final ML potential for (A) 9 set of supplemental training sets with equal proportion of cations and (B) 4 set of systems with unequal proportion of cations.**

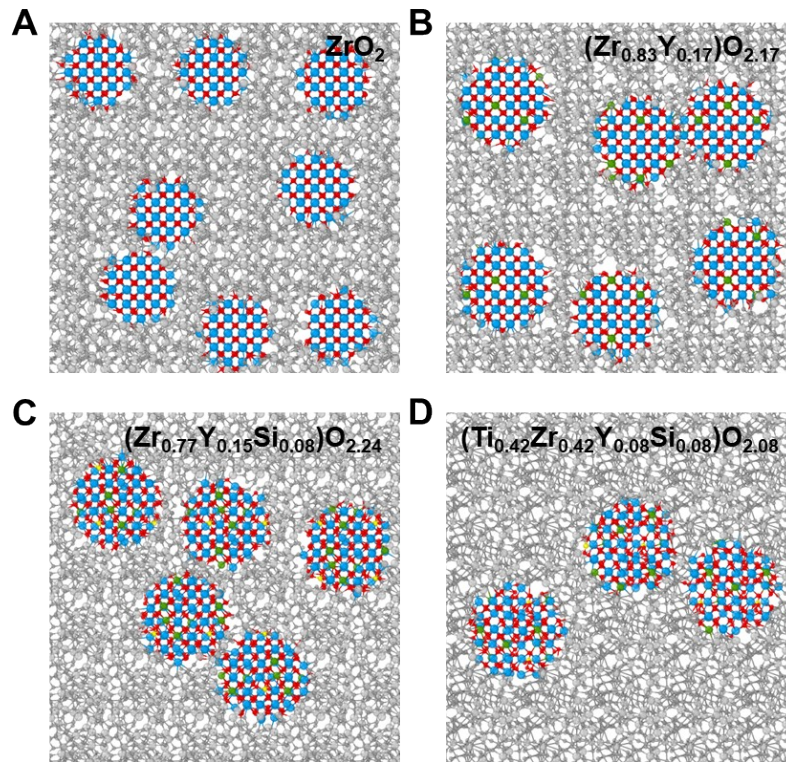


**Figure S4.**

**Initial states of the seeding simulation of the four systems. To reflect the difference in nucleation barrier, there are different numbers of nuclei at the initial stage in each system, 8 in (A),  $\text{ZrO}_2$ , 6 in (B),  $(\text{Zr}_{0.83}\text{Y}_{0.17})\text{O}_{2.17}$ , 5 in (C),  $(\text{Zr}_{0.77}\text{Y}_{0.15}\text{Si}_{0.08})\text{O}_{2.24}$ , and 3 in (D),  $(\text{Ti}_{0.42}\text{Zr}_{0.42}\text{Y}_{0.08}\text{Si}_{0.08})\text{O}_{2.08}$ .**

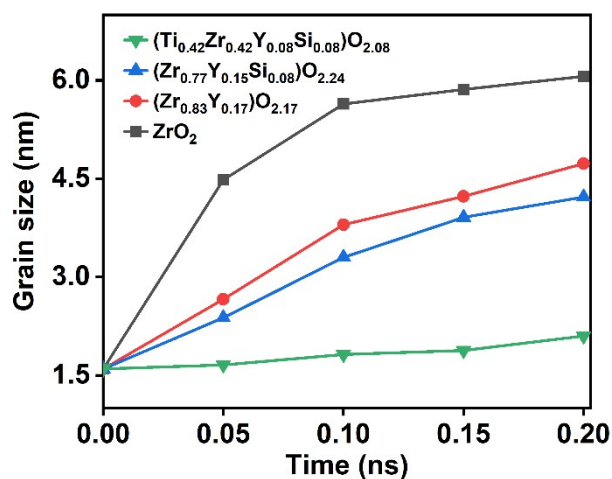


**Figure S5.**

**Time dependence of averaged grain size of medium-entropy ceramics comparing to three low-entropy ceramics by MD simulation.** The grain size in ZrO<sub>2</sub> was much higher due to the low diffusion barrier of Zr cation. The grain size in (Zr<sub>0.83</sub>Y<sub>0.17</sub>)O<sub>2.17</sub> was reduced due to the solute drag effects of Y<sup>3+</sup>. The silica further reduced grain size in (Zr<sub>0.77</sub>Y<sub>0.15</sub>Si<sub>0.08</sub>)O<sub>2.24</sub>, and the grain size in (Ti<sub>0.42</sub>Zr<sub>0.42</sub>Y<sub>0.08</sub>Si<sub>0.08</sub>)O<sub>2.08</sub> almost remained the original value.

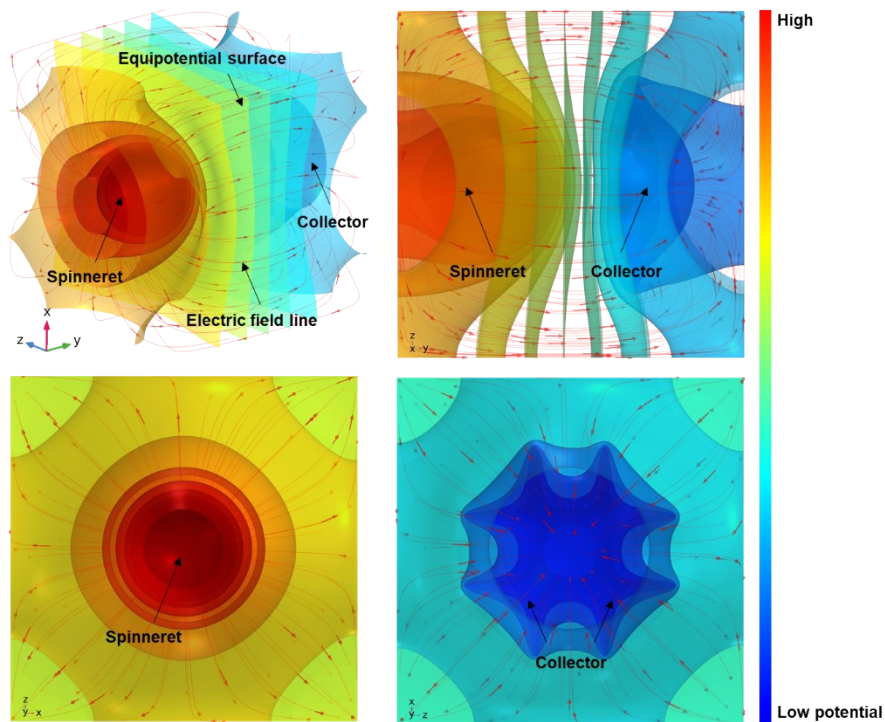


**Figure S6.**

**Electric field distribution map of FFE by COMSOL.** The spinneret and collector are annotated in the figure. Red lines with arrows indicated the electric field line. The surfaces with different color ranging from blue to red indicated the equipotential surface with increased potential. Pictures from different perspectives at spinneret, collector, and top view were given to illustrate the details.

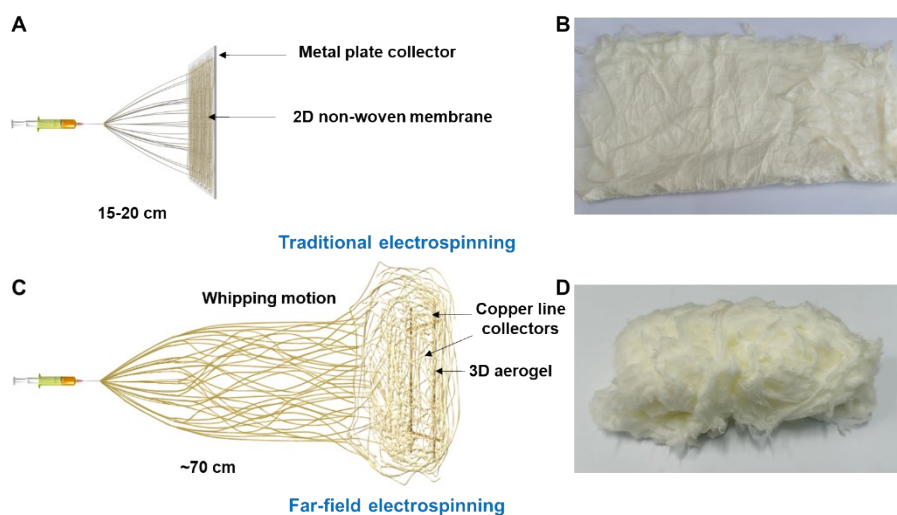


**Figure S7.**

**Differences between traditional electrospinning and far-field electrospinning.** (A) The schematic illustration of traditional electrospinning. (B) The optical image of 2D non-woven membrane by traditional electrospinning. (C) The schematic illustration of far-field electrospinning. (D) The optical image of 3D flurry aerogel obtained by far-field electrospinning. Traditional electrospinning tends to form 2D non-woven membrane deposited by electrospun fibers on the metal plate collector due to the strong electro field force. In comparison, far-field electrospinning could increase the entanglement between fibers and effectively reduce the electric field force at the linear collectors, forming the 3D porous structure of precursor aerogels.

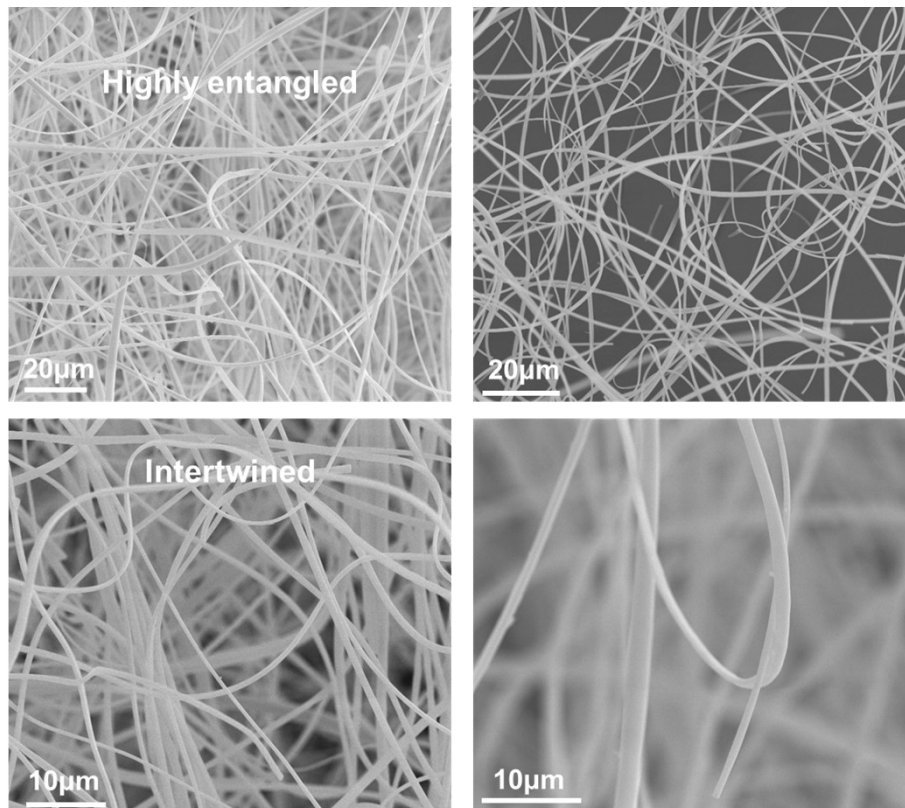


**Figure S8.** SEM images of ceramic fibrous aerogels fabricated via FFE with highly entangled and intertwined structure. The highly entangled fibrous network endowed the ceramic aerogels with exceptional deformation capability and fatigue resistance compared to the randomly stacking structure, which could lead to friction and sliding between adjacent fibers and severe structure degradation.



**Figure S9.**

**Optical images of the MECA.** (A) The as-spun fibrous aerogels with rectangular shape before calcination. (B) The MECA obtained by thermal calcination in air at 1,000 °C for 1h. (C) Diverse shapes of MECA.

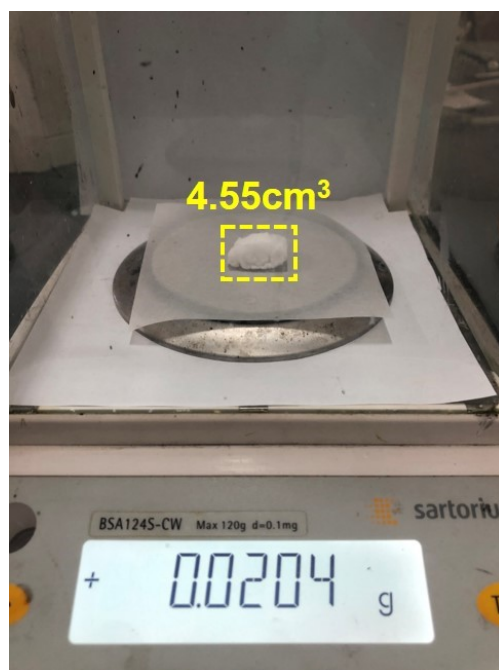


**Figure S10.**

**Density measurement of MECA (for example,  $4.48 \text{ mg cm}^{-3}$ ) with Micro balance.**



**Figure S11.**

**Optical images of low-entropy ceramic aerogels.** (A)  $\text{ZrO}_2$ , (B)  $(\text{Zr}_{0.83}\text{Y}_{0.17})\text{O}_{2.17}$ , (C)  $(\text{Zr}_{0.77}\text{Y}_{0.15}\text{Si}_{0.08})\text{O}_{2.24}$  fibrous aerogels.

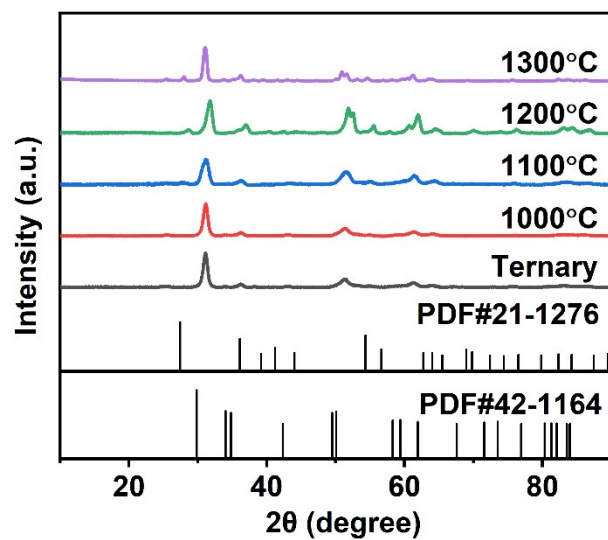


**Figure S12.**  
**XRD spectra of MECA calcined at different temperatures.**

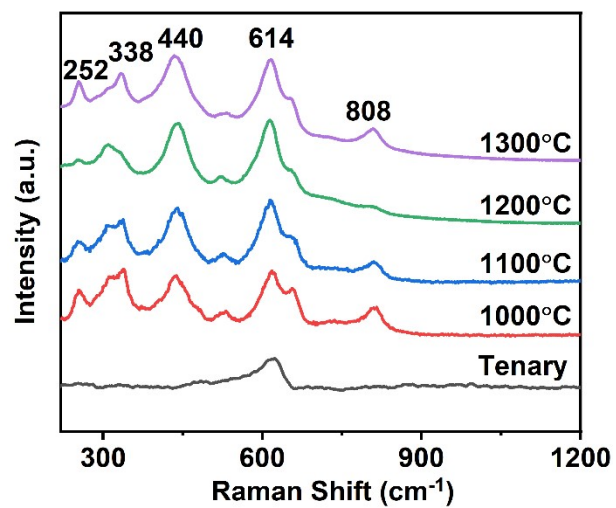


**Figure S13.**  
**Raman spectra of MECA calcined at different temperatures.**

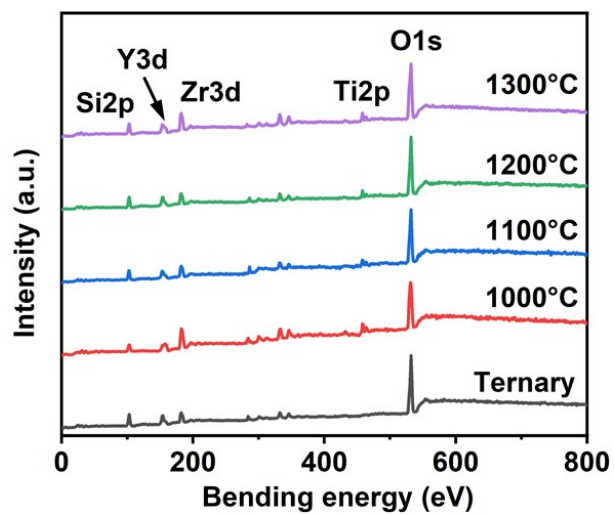


**Figure S14.**  
XPS spectra of MECA calcined at different temperatures.

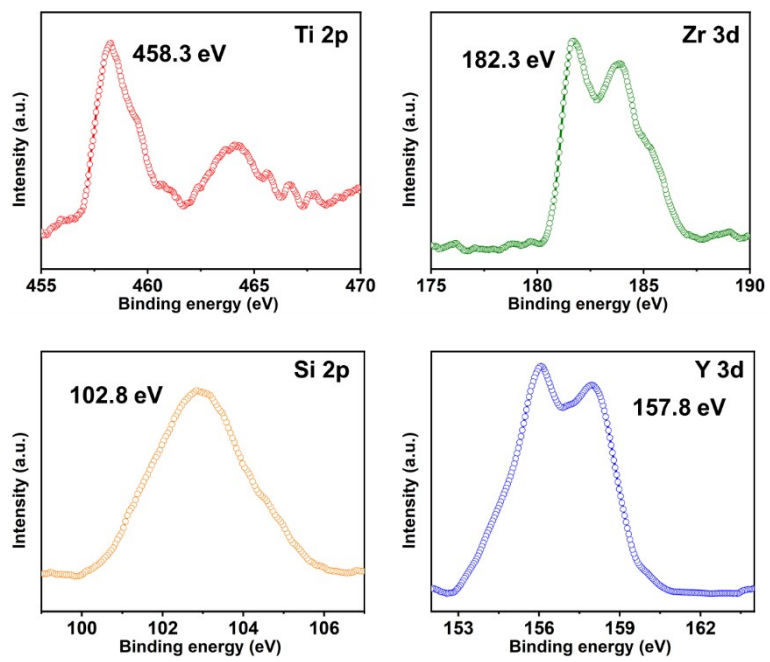


**Figure S15.**  
**Ti 2p, Zr 3d, Si 2p, and Y 3d XPS spectra of MECA.**

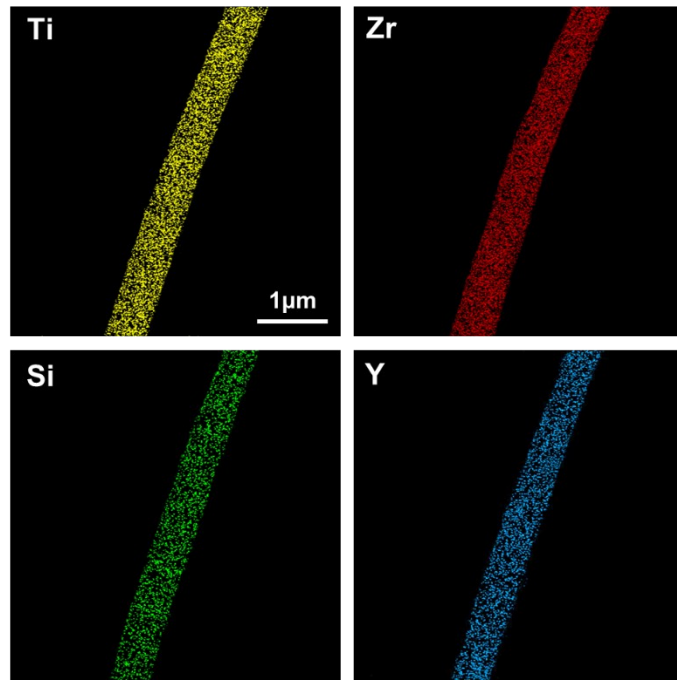


**Figure S16.**  
The SEM mapping of Ti, Zr, Si, Y, respectively.

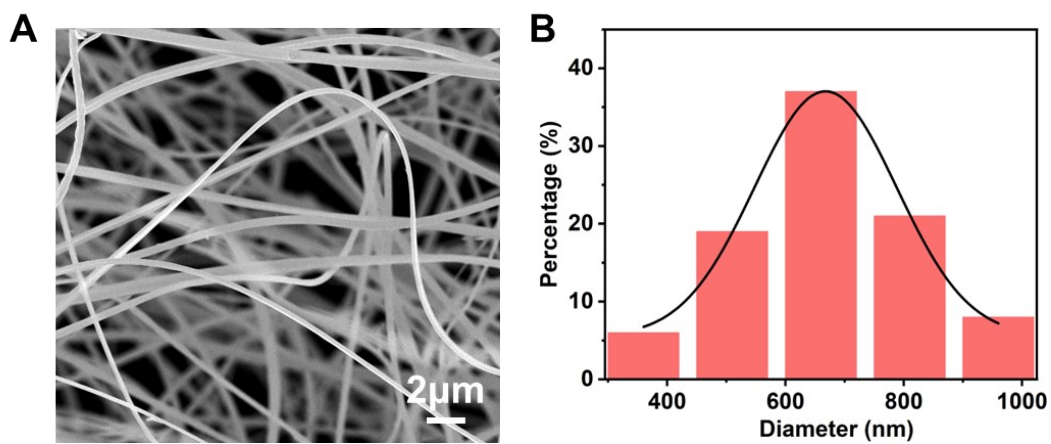


**Figure S17.**

(A) SEM image of the MECA. (B) Diameter distribution of the fibers.

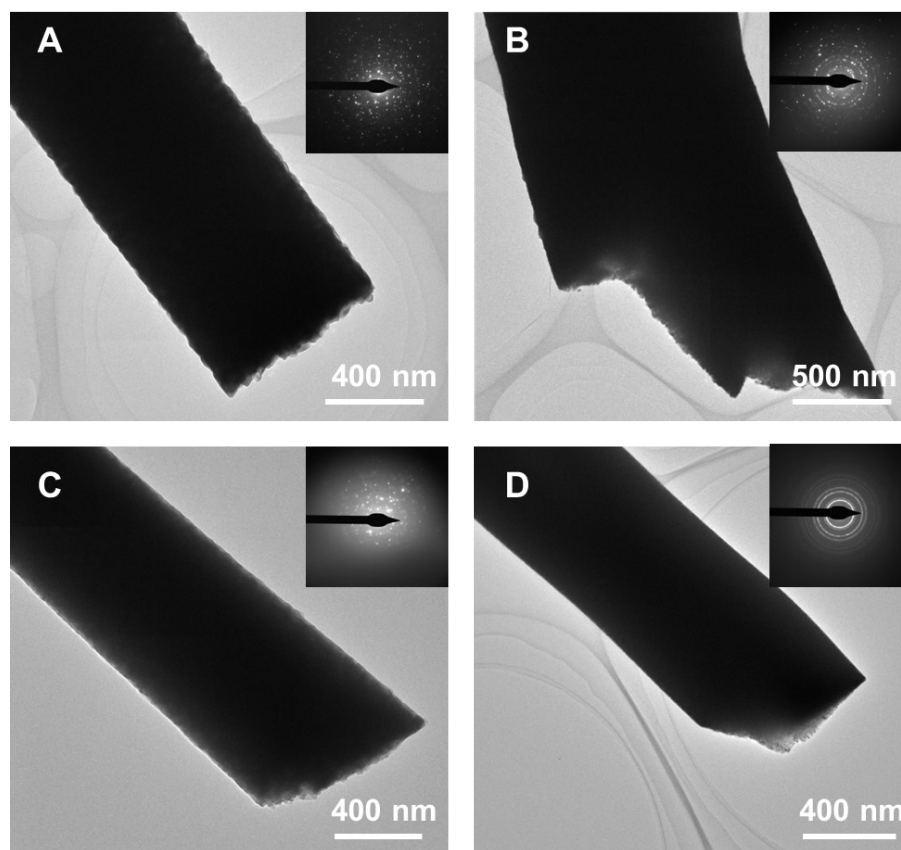


**Figure S18.**

**TEM images** of (A)  $\text{ZrO}_2$ , (B)  $(\text{Zr}_{0.83}\text{Y}_{0.17})\text{O}_{2.17}$ , (C)  $(\text{Zr}_{0.77}\text{Y}_{0.15}\text{Si}_{0.08})\text{O}_{2.24}$ , and (D)  $(\text{Ti}_{0.42}\text{Zr}_{0.42}\text{Y}_{0.08}\text{Si}_{0.08})\text{O}_{2.08}$ . Insets, the corresponding selected area electron diffraction (SAED).

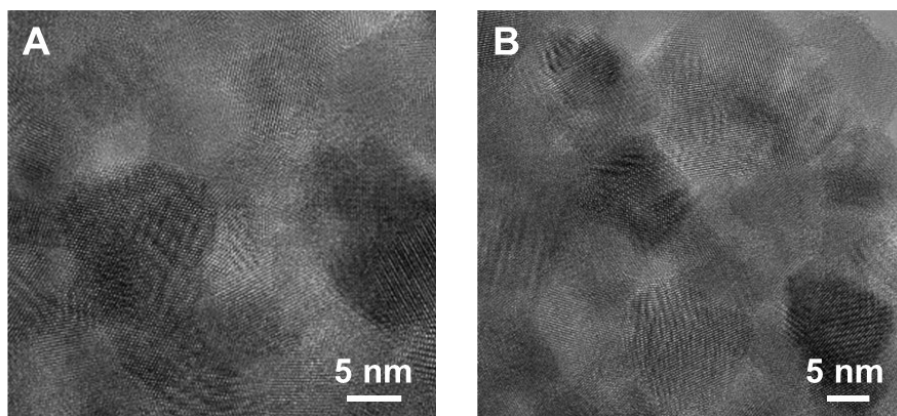


**Figure S19.**

**High resolution TEM images of MECA, indicating the polycrystalline structure with high lattice distortion.**

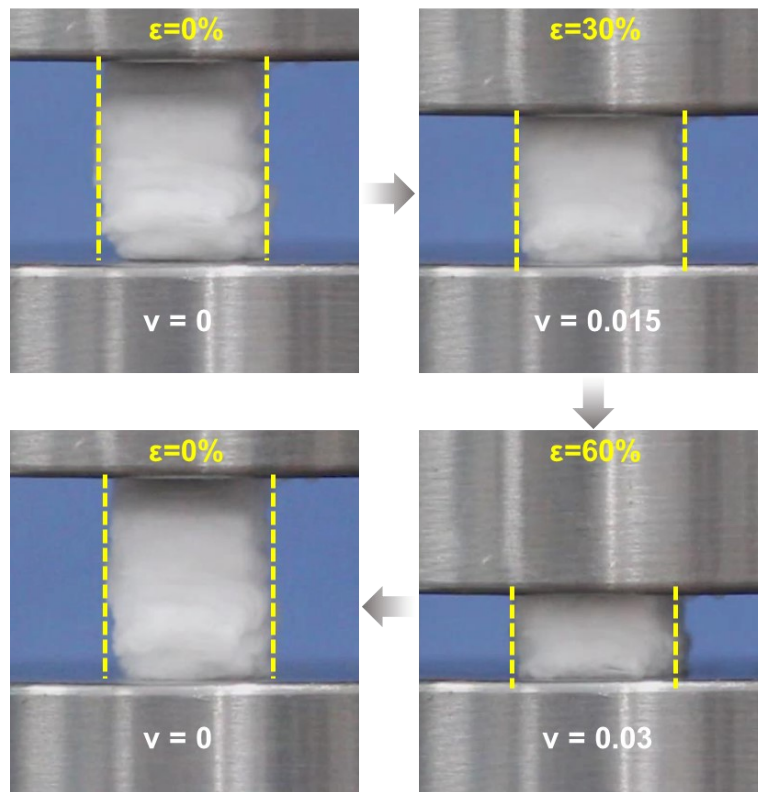


**Figure S20.**  
**Optical images of MECA with near-zero  $\nu$  at different strain.**

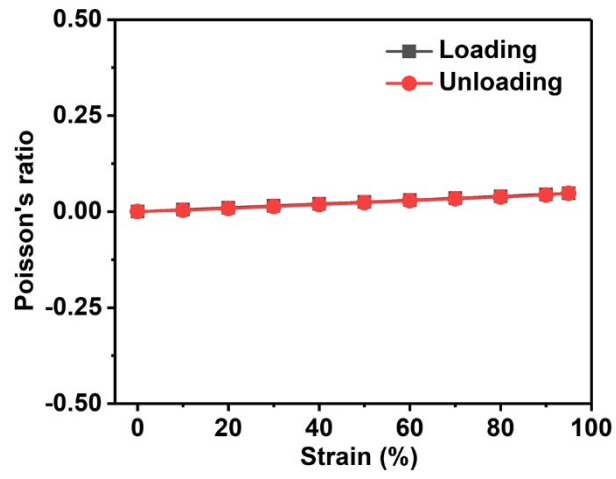


**Figure S21.**  
 **$\nu$  of MECA under strain during loading and unloading.**

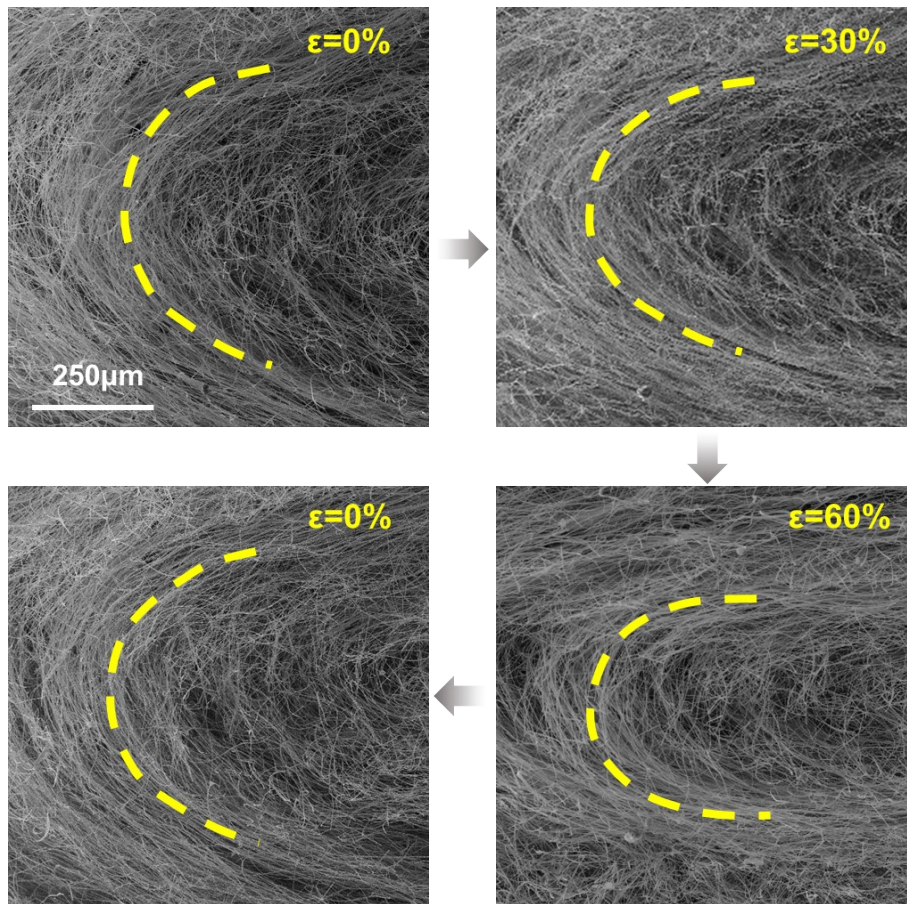


**Figure S22.**

**SEM images of *in situ* compression test of MECA.** The bending corner formed by curved fibers could support the compressive stress and storage the elastic potential energy. With increasing compression strain, the curvature of the fibers gradually decreased. After the removal of external stress, the curved fibers could provide additional resilience compared to lamellar structure.

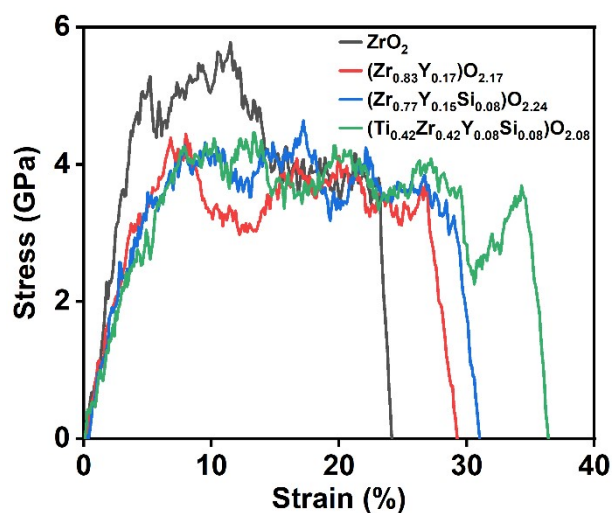


**Figure S23.**

**MD fracture simulations of  $\text{ZrO}_2$ ,  $(\text{Zr}_{0.83}\text{Y}_{0.17})\text{O}_{2.17}$ ,  $(\text{Zr}_{0.77}\text{Y}_{0.15}\text{Si}_{0.08})\text{O}_{2.24}$ , and  $(\text{Ti}_{0.42}\text{Zr}_{0.42}\text{Y}_{0.08}\text{Si}_{0.08})\text{O}_{2.08}$  fibers.** The fracture strain of MECA fiber is enhanced compared to other fibers, while there is no increase in fracture stress. Because the incorporation of  $\text{TiO}_2$  could generate softening effects and compromise the mechanical strength of ceramic fibers. We adopted the medium-entropy strategy to overcome the softening effect of the  $\text{TiO}_2$ , and enhance the fracture strain while maintaining the fracture stress.

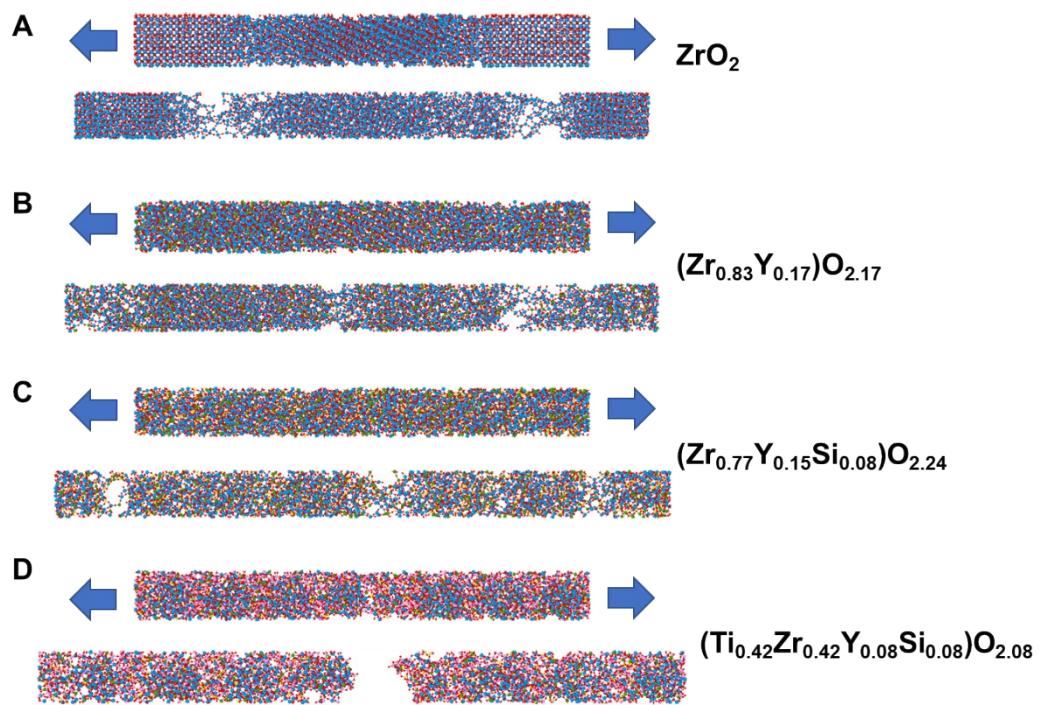


**Figure S24.**

**MD fracture simulation images of fiber of (A)  $\text{ZrO}_2$ , (B)  $(\text{Zr}_{0.83}\text{Y}_{0.17})\text{O}_{2.17}$ , (C)  $(\text{Zr}_{0.77}\text{Y}_{0.15}\text{Si}_{0.08})\text{O}_{2.24}$ , (D)  $(\text{Ti}_{0.42}\text{Zr}_{0.42}\text{Y}_{0.08}\text{Si}_{0.08})\text{O}_{2.08}$ .**

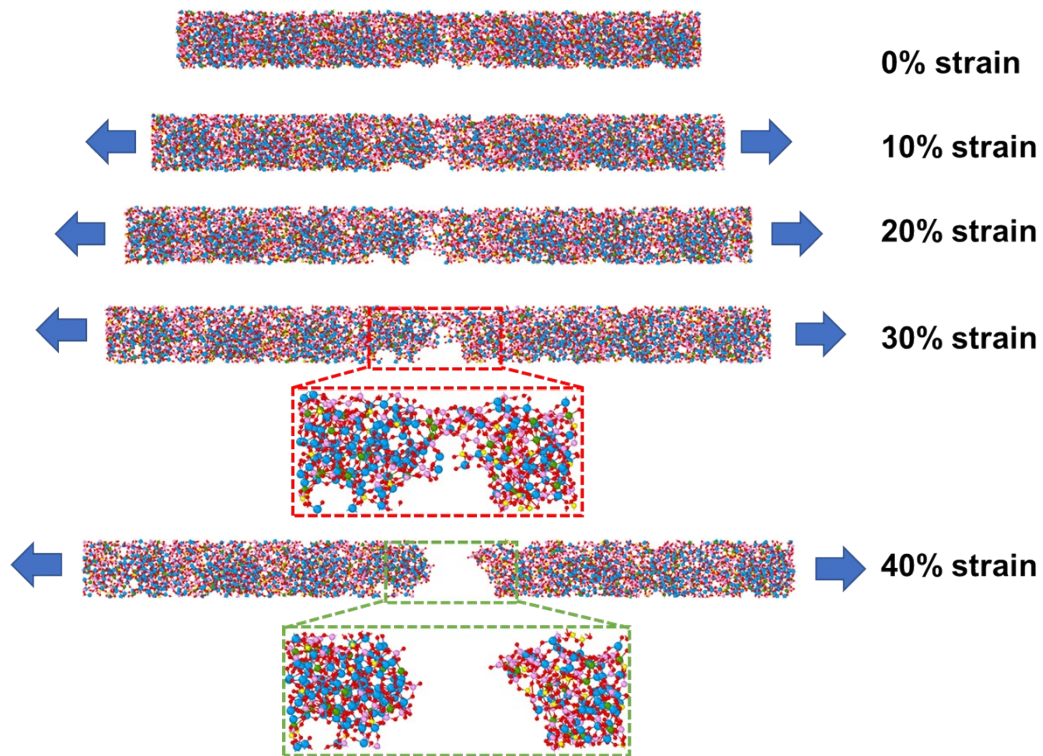


**Figure S25.**

**MD fracture simulation images of nanofiber of  $(\text{Ti}_{0.42}\text{Zr}_{0.42}\text{Y}_{0.08}\text{Si}_{0.08})\text{O}_{2.08}$  under tensile strain from 0% to 40%.** The grains in the quaternary system are much smaller compared to other systems. The abundant boundaries could perform as lubrication region, enhancing the deformability of the fibers. With the grain growth, the large-grained region would lead to concentrated external stress and catastrophic failure with reduced deformability.

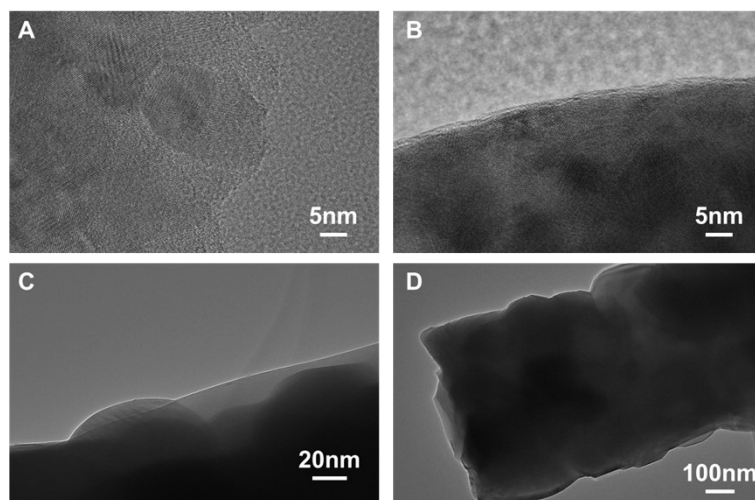


**Figure S26.**  
**TEM images of MECA prepared by different calcination temperatures (A) 1,000 °C, (B) 1,100 °C, (C) 1,200 °C, (D) 1,300 °C.**

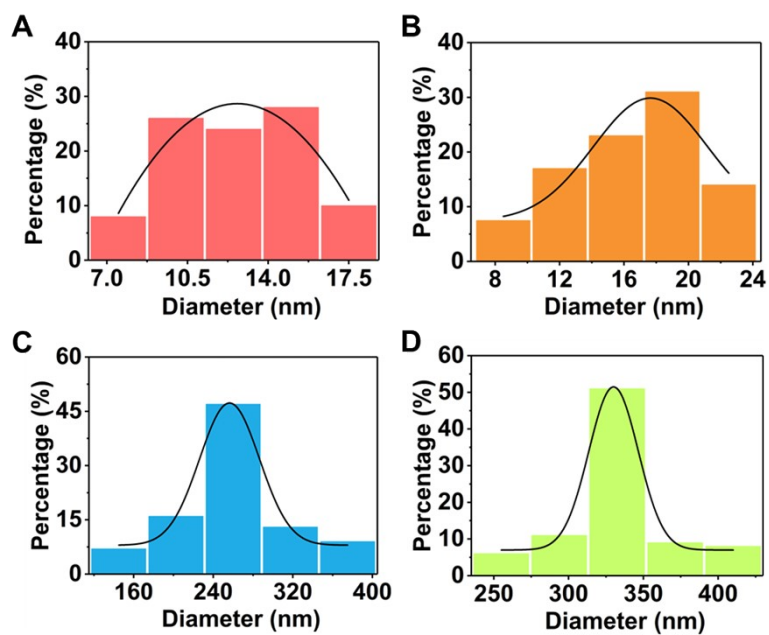


**Figure S27.**  
**Size distributions of the grains of the fiber prepared by different calcination temperatures (A) 1,000 °C, (B) 1,100 °C, (C) 1,200 °C, (D) 1,300 °C.**

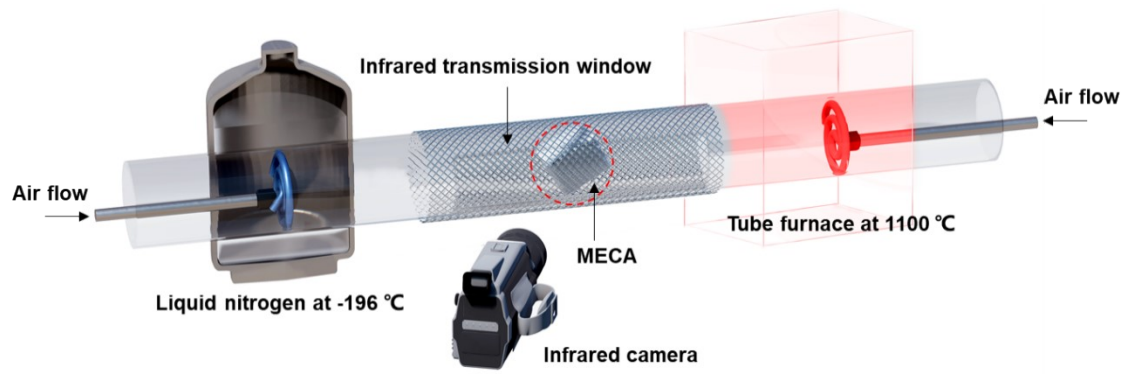


**Figure S28.**

**Home-design pneumatic apparatus for thermal shock test of MECA.** The tube furnace was used as a hot end at  $1,100\text{ }^{\circ}\text{C}$ . Liquid nitrogen was used as a cold end at  $-196\text{ }^{\circ}\text{C}$ . The sample was drove back and forth between the hot and cold ends by air flow.

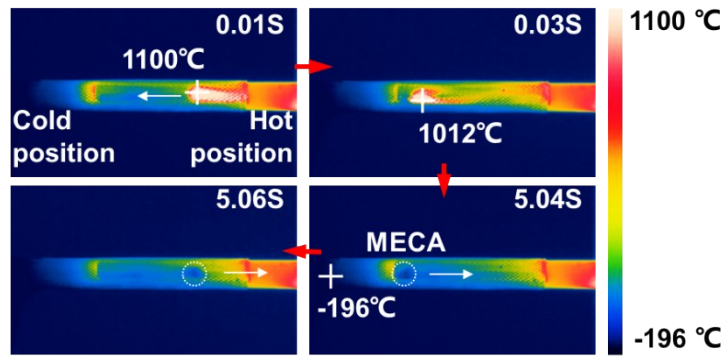


**Figure S29.**  
Infrared images of one thermal shock cycle of MECA with temperature swing up to ~1,300 °C.

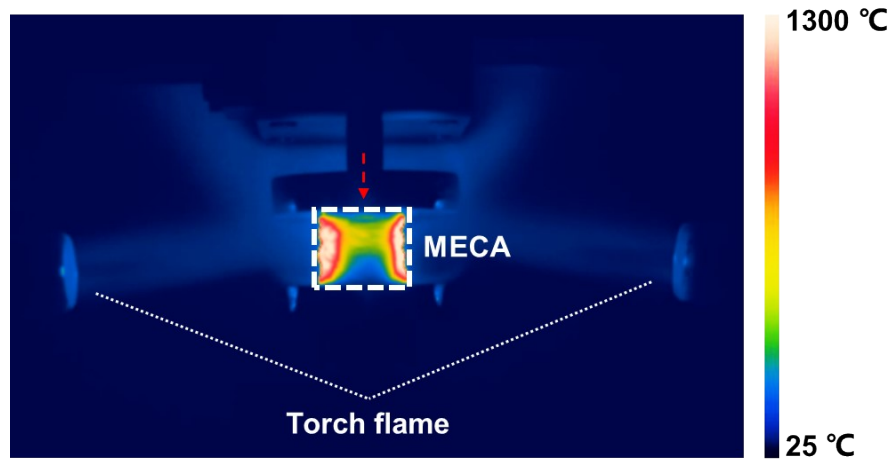


**Figure S30.**  
**Infrared images of MECA compressed at cyclic strain of 50% under torch blowing flames.**

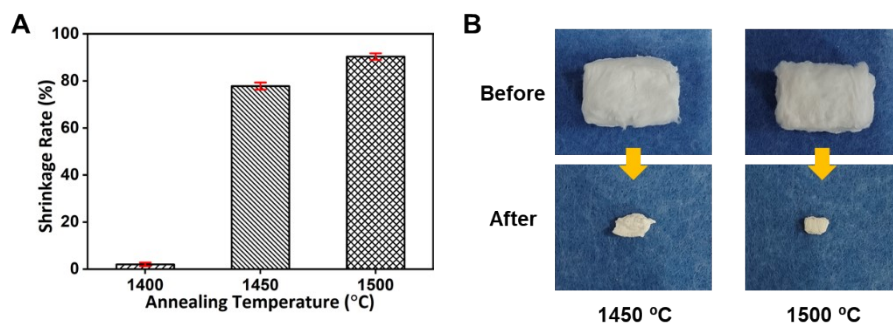


**Figure S31.**

**MECA annealed at 1450 and 1500 °C for 1h.** (A) Shrinkage rate of MECA annealed at different temperature, (B) Optical images of MECA annealed before 1450 and 1500 °C.

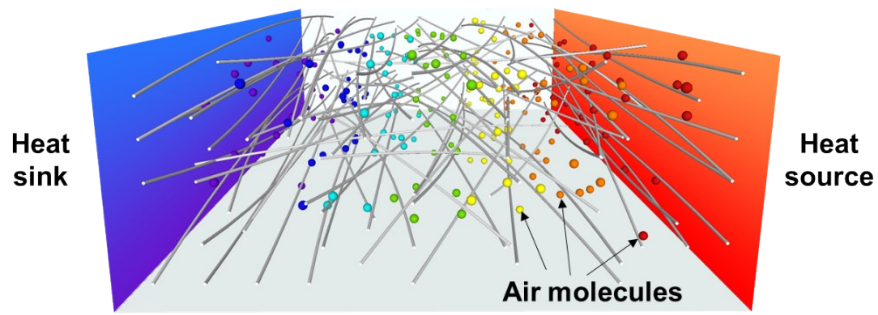


**Figure S32.**

**Illustration of heat transfer of ceramic fibrous aerogels.** Air molecules with mean free path over 70 nm in fibrous aerogels could transfer heat by thermal motion or collision with each other, and are the main source of heat transfer at temperature below 100 °C.

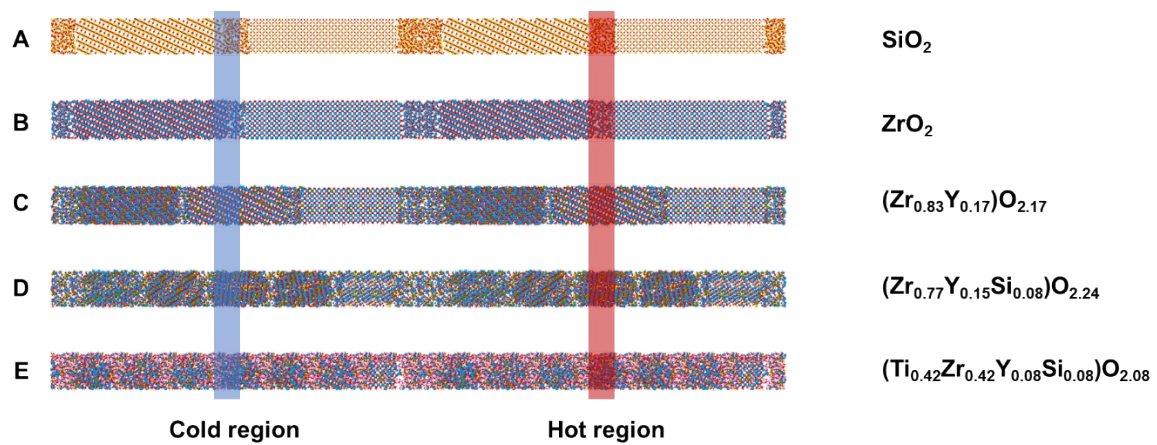


**Figure S33.**

**MD simulation of solid conduction** in (A)  $\text{SiO}_2$ , (B)  $\text{ZrO}_2$ , (C)  $(\text{Zr}_{0.83}\text{Y}_{0.17})\text{O}_{2.17}$ , (D)  $(\text{Zr}_{0.77}\text{Y}_{0.15}\text{Si}_{0.08})\text{O}_{2.24}$ , and (E)  $(\text{Ti}_{0.42}\text{Zr}_{0.42}\text{Y}_{0.08}\text{Si}_{0.08})\text{O}_{2.08}$  fibers.

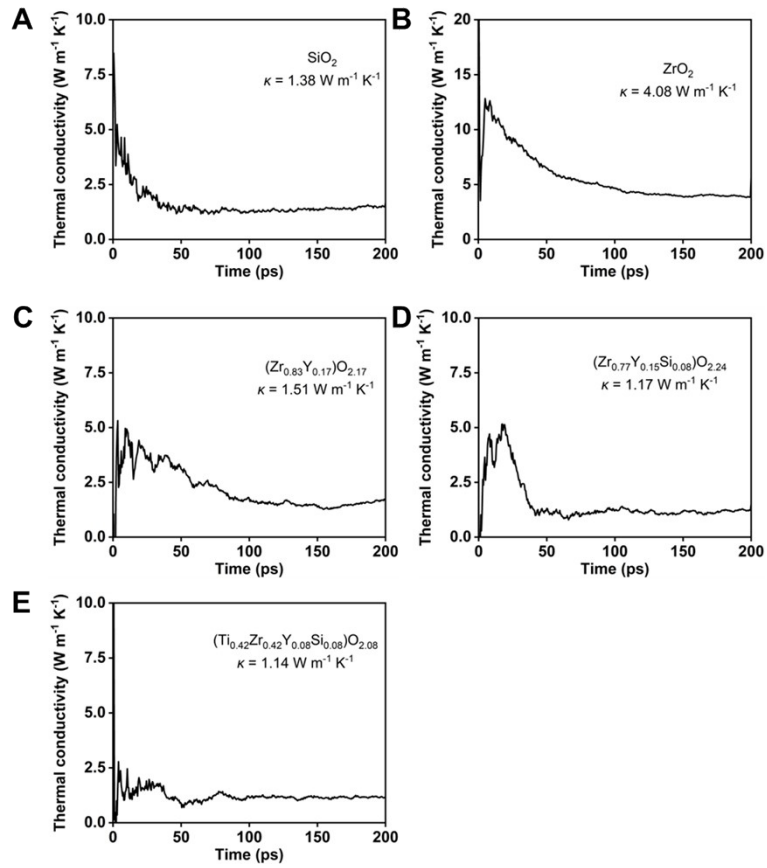


**Figure S34.**

**Time dependence of  $\kappa$ , of (A)  $\text{SiO}_2$ , (B)  $\text{ZrO}_2$ , (C)  $(\text{Zr}_{0.83}\text{Y}_{0.17})\text{O}_{2.17}$ , (D)  $(\text{Zr}_{0.77}\text{Y}_{0.15}\text{Si}_{0.08})\text{O}_{2.24}$ , (E)  $(\text{Ti}_{0.42}\text{Zr}_{0.42}\text{Y}_{0.08}\text{Si}_{0.08})\text{O}_{2.08}$  fibers along axial direction.**

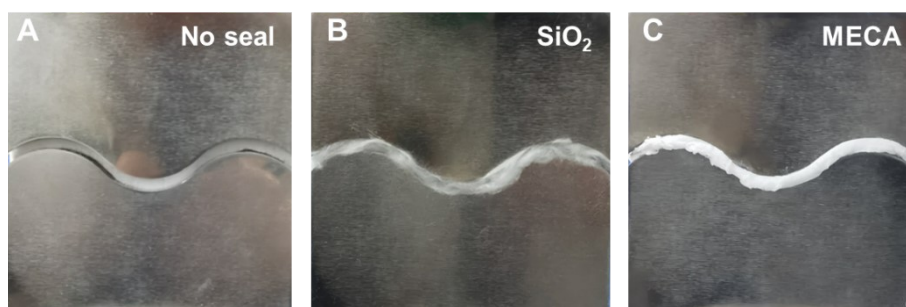


**Figure S35.**

**Thermal sealing performance** of (A) no seal, (B) SiO<sub>2</sub> commercial seal, and (C) MECA.

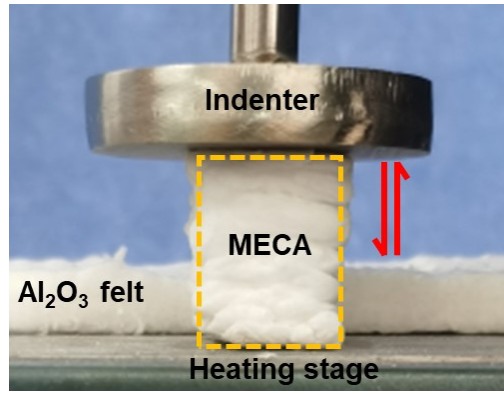


**Figure S36.**  
**Thermal sealing performance of MECA with large amplitude vibration.**

**Table S1.** Details of the collected configurations during stepwise training procedure of the ML potential for the medium-entropy ceramic system.

Iter	System	No. atoms	No. candidate configurations	Candidate Percentage
0	$(\text{Ti}_{0.42}\text{Zr}_{0.42}\text{Y}_{0.08}\text{Si}_{0.08})\text{O}_{2.08}$	130	4308	33.06
1	$(\text{Ti}_{0.42}\text{Zr}_{0.42}\text{Y}_{0.08}\text{Si}_{0.08})\text{O}_{2.08}$	130	8894	/
	$\text{ZrO}_2$	108	2142	11.51
	$\text{Y}_2\text{O}_3$	90	1179	6.60
	$\text{SiO}_2$	108	894	4.98
	$\text{TiO}_2$	108	462	2.15
2	$(\text{Ti}_{0.42}\text{Zr}_{0.42}\text{Y}_{0.08}\text{Si}_{0.08})\text{O}_{2.08}$	130	1144	/
	$\text{ZrTiO}_4$	108	993	3.87
	$\text{Zr}_2\text{Y}_2\text{O}_7$	99	596	5.85
	$\text{ZrSiO}_4$	108	1594	5.00
	$\text{ZrO}_2$	108	1070	/
	$\text{Y}_2\text{O}_3$	90	2303	/
	$\text{SiO}_2$	108	1735	/
	$\text{TiO}_2$	108	675	/
3	$(\text{Ti}_{0.42}\text{Zr}_{0.42}\text{Y}_{0.08}\text{Si}_{0.08})\text{O}_{2.08}$	130	816	/
	$\text{ZrTiSiO}_6$	108	1047	1.98
	$\text{Zr}_2\text{Y}_2\text{Ti}_2\text{O}_{11}$	102	1047	1.98
	$\text{ZrTiO}_4$	108	1047	/
	$\text{Zr}_2\text{Y}_2\text{O}_7$	99	2492	/
	$\text{ZrSiO}_4$	108	1046	/
	$\text{ZrO}_2$	108	2863	/
4	$(\text{Ti}_{0.42}\text{Zr}_{0.42}\text{Y}_{0.08}\text{Si}_{0.08})\text{O}_{2.08}$	130	2282	/
	$\text{ZrO}_2$	96	827	3.00
	$(\text{Zr}_{0.83}\text{Y}_{0.17})\text{O}_{2.17}$	128	1374	2.60
	$(\text{Zr}_{0.77}\text{Y}_{0.15}\text{Si}_{0.08})\text{O}_{2.24}$	118	3768	7.15
5	$(\text{Ti}_{0.42}\text{Zr}_{0.42}\text{Y}_{0.08}\text{Si}_{0.08})\text{O}_{2.08}$	189	831	1.58
	$\text{ZrO}_2$	96	759	/
	$(\text{Zr}_{0.83}\text{Y}_{0.17})\text{O}_{2.17}$	93	2905	5.50
	$(\text{Zr}_{0.77}\text{Y}_{0.15}\text{Si}_{0.08})\text{O}_{2.24}$	111	1683	3.19
Total			52776	100.00

For each iteration, we report the number of atoms, the number of selected configurations, and the candidate percentage of each system among the whole training data set.

**Movie S1.**

Compression test of MECA at 95% strain.

**Movie S2.**

Cyclic compression test of MECA at 50% strain.

**Movie S3.**

Tensile test of MECA.

**Movie S4.**

Bending test of MECA.

**Movie S5.**

Thermal shock test of MECA.

**Movie S6.**

Thermoelasticity of MECA under torch flame.

**Movie S7.**

Thermal sealing performance of MECA.

**Movie S8.**

Thermal sealing performance of MECA under large amplitude vibration.

## REFERENCES AND NOTES

- 1 G. C. Sosso, J. Chen, S. J. Cox, M. Fitzner, P. Pedevilla, A. Zen and A. Michaelides, *Chem. Rev.*, 2016, **116**, 7078–7116.
- 2 G. M. Torrie and J. P. Valleau, *J. Comput. Phys.*, 1977, **23**, 187–199.
- 3 A. Laio and M. Parrinello, *Proc. Natl. Acad. Sci.*, 2002, **99**, 12562–12566.
- 4 O. Valsson, P. Tiwary and M. Parrinello, *Annu. Rev. Phys. Chem.*, 2016, **67**, 159–184.
- 5 A. Barducci, G. Bussi and M. Parrinello, *Phys. Rev. Lett.*, 2008, **100**, 020603.
- 6 S. Angioletti-Uberti, M. Ceriotti, P. D. Lee and M. W. Finnis, *Phys. Rev. B*, 2010, **81**, 125416.
- 7 B. Cheng, G. A. Tribello and M. Ceriotti, *Phys. Rev. B*, 2015, **92**, 180102.
- 8 P. J. Steinhardt, *Phys. Rev. B*, 1983, **28**, 784–805.
- 9 P.-R. ten Wolde, M. J. Ruiz-Montero and D. Frenkel, *Faraday Discuss.*, 1996, **104**, 93–110.
- 10 I. Ronneberger, W. Zhang, H. Eshet and R. Mazzarello, *Adv. Funct. Mater.*, 2015, **25**, 6407–6413.
- 11 J. Behler, *J. Chem. Phys.*, 2016, **145**, 170901.
- 12 L. Bonati and M. Parrinello, *Phys. Rev. Lett.*, 2018, **121**, 265701.
- 13 H. Niu, L. Bonati, P. M. Piaggi and M. Parrinello, *Nat. Commun.*, 2020, **11**, 2654.
- 14 B. Guillot and N. Sator, *Geochim. Cosmochim. Acta*, 2007, **71**, 1249–1265.
- 15 J. Du, *J. Am. Ceram. Soc.*, 2009, **92**, 87–95.
- 16 J. Du, R. Devanathan, L. R. Corrales, W. J. Weber and A. N. Cormack, *Phys. Rev. B*, 2006, **74**, 214204.